2.5 He IMPLANTATION OF Fe–{110}YTO BILAYERS — T. Stan, Y. Wu, T. Brown, C. Palmstrom, and G.R. Odette (University of California Santa Barbara), and F. Allen, P. Hosemann (University of California Berkeley)

OBJECTIVE

The objective of this work is to fabricate mesoscale Fe-$Y_2Ti_2O_7$ interfaces in the form of bilayers that are amenable to detailed characterization techniques and He implantation experiments.

SUMMARY

The Fe-Cr matrix nanostructured ferritic alloys (NFAs) are dispersion strengthened by < 5 nm Y-Ti-O nano-oxide (NO) phases. The characteristics of the interfaces between the NOs, such as $Y_2Ti_2O_7$ (YTO), and the surrounding ferrite matrix are critical to trapping He in fine scale bubbles. As a compliment to current characterization efforts of the NOs themselves, a surrogate bulk Fe-YTO interface was fabricated by molecular beam epitaxy (MBE) and electron beam Fe deposition on {110}YTO. Areas of the sample were then implanted with 25 keV He. The He bubble sizes, number densities, and volume fractions are reported. Bubbles at the Fe-YTO interface were on average larger than in the matrix. No bubbles were seen in, but this does not indicate that He is not present in the YTO.

PROGRESS AND STATUS

Introduction

Materials for nuclear fusion applications must reliably perform at high temperatures and manage high levels of helium (He). Nanostructured Ferritic Alloys (NFAs) are a promising class of Fe-Cr-based stainless steels that have remarkable mechanical properties, are thermally stable up to 1000 °C, and are irradiation tolerant [1-3]. NFAs contain a high density (~$10^{23}/m^2$) of 2-3 nm Y-Ti-O nano-oxides (NOs) which help impede dislocation climb and glide, stabilize dislocation and grain structures, and trap He in fine-scale bubbles at matrix-NO interfaces, preventing void swelling and He embrittlement. Indeed, NFAs may turn He from a liability to an asset. For example, He bubbles act as recombination sites for vacancies and interstitials, thus promoting self-healing. The high density of matrix-NO interfaces prevents He from collecting at grain boundaries, which would otherwise degrade creep and fracture properties.

There is ongoing research to determine the compositions, structures, and orientation relationships (ORs) for the NOs themselves. A summary of these studies and other NFA properties was recently published by Odette [1]. The most common reported NO is $Y_2Ti_2O_7$ (YTO) fcc pyrochlore. Characterization and analysis of the NO-matrix interfaces is needed to develop first principles and atomic interface models that predict NFA performance in fusion reactor environments. YTO-matrix ORs are of interest because they affect interface defect structures, misfit strains, and energies.

The NO-matrix interfaces are difficult to characterize in NFAs using conventional microscopy techniques due to the nm size scale. The research approach in this study is to deposit Fe on bulk oriented YTO single crystal substrates to create surrogate mesoscopic-scale interfaces. Even if the bilayers do not have same characteristics as the embedded ones, this study will further the general understanding of metal-oxide interfaces. Bilayers are also amenable to irradiation studies such as interactions with point defects and He.

Studies of Fe deposited on {111}YTO were previously published by Stan et al. [7], while Fe on {100}YTO and {110}YTO were reported in other Fusion Semi Annual Reports [8-10]. This study is a continuation of the previous results by characterizing a new Fe deposition on {110}YTO, and the associated He implantation.

Experimental Procedure

The details of sample fabrication and the characterization instruments used are covered in a previous publication [7]. In summary, a YTO single crystal was grown by the Chelkowski method at University of Tennessee. The crystal was then {110} surface oriented and 2 mm thick wafers were cut. An Allied Multiprep instrument was used to polish the wafer using a sequence of diamond lapping films, followed by a final 15 minute polishing step using a 0.02 µm non-crystallizing colloidal silica suspension. The wafer was placed under running deionized (DI) water, followed by a sequential series of 5 min sonic bath treatments in: 10 vol% Micro-Organic soap and 90 vol% DI water, acetone, isopropanol, and finally DI water.

The Fe film was grown in the UCSB Palmstrom laboratory interconnected molecular beam epitaxy (MBE) system. The wafer was inserted into the system and pumped down to ultra-high vacuum (~10^{-11} Torr). The substrate was then outgassed by annealing at 700 ^{o}C for 1 hour. The first 20 nm of Fe were MBE grown at room temperature. The first 5 nm were grown slowly with a deposition rate of 0.5 Å/min, while the remaining 15 nm were grown with a faster rate of 1.35 Å/min. The sample was then annealed at 300 ^{o}C for 1 hour to allow the film to equilibrate. An extra 200 nm of Fe was then deposited on top of the MBE-grown layer using an electron beam system with 2 Å/sec at 300 ^{o}C. The 220 nm Fe layer was capped with 5 nm of electron beam grown AlO_x to prevent Fe oxidation. The Fe-YTO bilayer was then moved into an Oxford FlexAL assisted layer deposition (ALD) instrument at the UCSB Nanofab facility. 9 nm of Pt was uniformly deposited on the entire sample. In total, the sample is composed of 2 mm thick YTO, 220 nm Fe, 5 nm AlO_x, and 9 nm Pt.

The sample was then He implanted using a 25 keV ion beam using a Zeiss ORION NanoFab microscope at UC Berkeley. A 10 pA beam was rastered over a 10 x 10 µm area, with the sample tilted at 7° to prevent channeling, for a total dose of 4E15 He/cm^2. Stopping and Range of Ions in Matter (SRIM) simulations indicate a peak concentration of ~2000 ppm He at a depth of 120 nm into the Fe film, and a total implantation range of ~200 nm, roughly the same as the total Fe film thickness.

The bilayer was characterized using an FEI Quanta 400F field-emission scanning electron microscope (SEM) with an electron backscatter diffraction (EBSD) detector. The sample was placed into an FEI HELIOS Focus Ion Beam (FIB) tool and 5 µm of protective platinum were deposited over areas of interest. Lift-outs <30 nm thick of the Fe-YTO interface were extracted, and a low energy 2 keV 5.5 pÅ gallium beam was used for the final cleaning. Transmission electron microscopy (TEM) observations were performed on a 300 keV FEI Titan.

Results

<u>SEM and EBSD Characterization</u>

Figure 1 shows EBSD data from the Fe film. Figure 1a is an EBSD band contrast (BC) image showing the Fe grain sizes and shapes. The sub-micron grains range in size from ~20 nm to ~200 nm. Figure 1b shows an EBSD inverse pole figure (IPF) map depicting the out-of-plane crystallographic orientation of the Fe grains. The range of colors indicates no clear preferred texturing normal to the film surface. Figure 1c shows the same data as Figure 1b but represented as Euler maps indicating the full orientation of the Fe grains. The large variation in coloring indicates no preferred in-plane orientation.

Figure 1d shows four pole figures (<100>, <110>, <111> and <112> reflections) of the data from the IPF map in Figure 1b, colored according to the out-of-plane grain orientation (IPFZ). The streaks in the pole figures (PFs) indicate axiotaxial texturing, and are further seen in the contour PFs in Figure 1e. This texturing is characterized by the alignment of planes in the Fe grain and in the YTO substrate that lie off-normal to the sample surface. Axiotaxial texturing results in an interface that is periodic in one dimension. The red spot in the <110>Fe PF in Figure 1e indicates a high concentration of aligned planes. PFs from the {110}YTO substrate are represented in Figure 1f. The off-centered green spot in

the <100>YTO PF overlaps with that seen for <110>Fe, but not at the same distance away from the center. Thus, the axiotaxial matching is close to <110>Fe\\<100>YTO. Last, Figure 1g shows 3D renderings of some selected Fe grains, and the {110}YTO substrate.

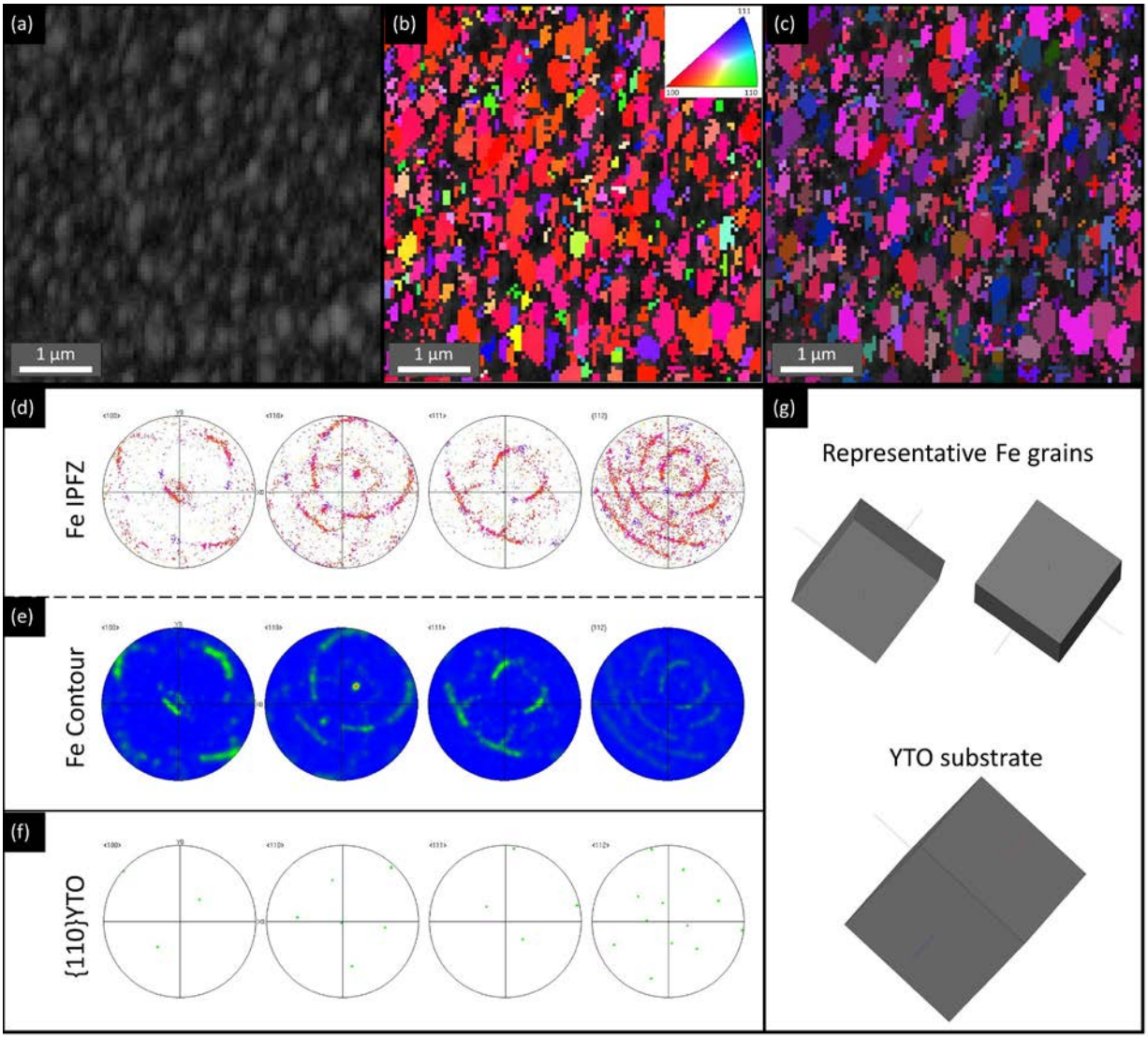

Figure 1. a) Band contrast, b) inverse pole figure map and c) Euler map of the Fe film. d) Fe pole figures colored according to the out-of-plane orientation, and e) contour mapping. f) YTO substrate pole figures. g) 3D renderings of some Fe grains (top two) and YTO substrate (bottom).

TEM Characterization

Transmission electron microscopy was used to characterize the He-implanted Fe film. Figure 2a is a schematic showing the Pt + AlO_x coating, four Fe grains, and {110}YTO substrate for the TEM micrographs in over-focus (Figure 2b) and under-focus (Figure 2c) conditions. He bubbles are seen as dark dots in the over-focus condition, and as white dots in the under-focus condition. Bubbles are found within the Fe grains and at all boundaries including AlO_x-Fe, Fe-Fe grain boundaries, and Fe-YTO interface. No bubbles were observed in the YTO substrate, however, this does not mean that He did not reach the YTO substrate (discussed later).

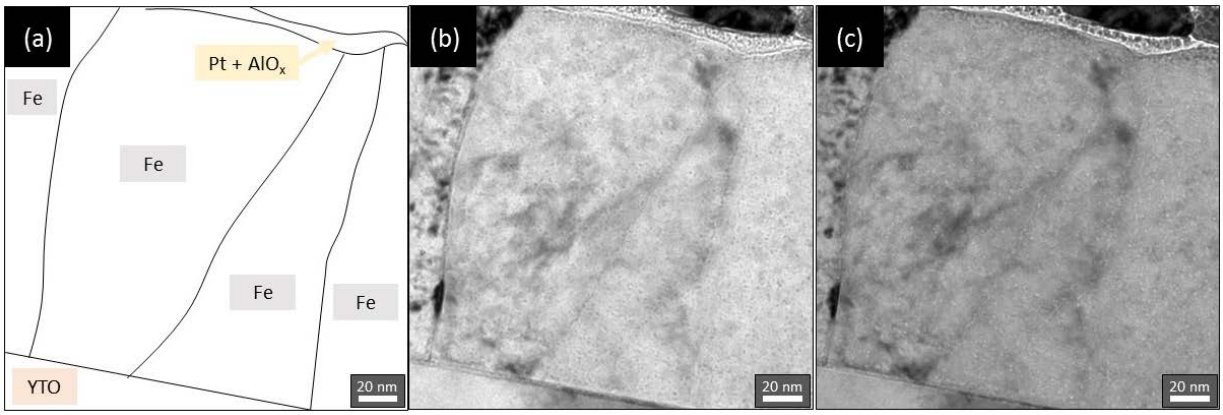

Figure 2. a) Schematic showing the Pt + AlO_x coating, four Fe grains, and YTO substrate for the b) over-focus and c) under-focus TEM images.

Figure 3 is a TEM image taken from the top half of an Fe grain. The red circles indicate the size and location of He bubbles. The bubble number density and volume fraction was calculated as a function of depth by first splitting the image into 10 nm tall and 90 nm wide sections, indicated by the white boxes in Figure 3. The top-most 10 nm box shows the He bubble distribution close to the AlO_x-Fe interface. It has a high number density of small He bubbles. However, not all grains had this bubble-rich area. This effect may be due to the axiotaxy, which causes the crystallographic Fe orientation to vary from grain to grain. The area between 10 nm and 20 nm has fewer but larger bubbles. Below the 20 nm depth, the average bubble size and number density generally increases. This is consistent with SRIM calculations that indicate a peak He concentration at ~120 nm.

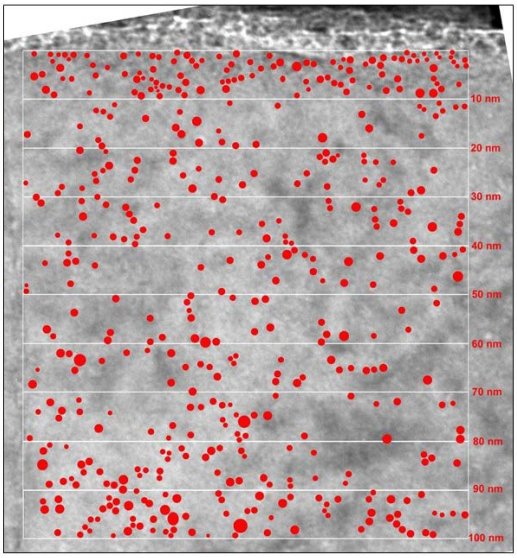

Figure 3. TEM image from an Fe grain. Red circles show the sizes and locations of He bubbles. The Fe-YTO interface is not shown in this image.

The under-focus TEM image in Figure 4 shows part of the Fe-YTO interface. A total of 26 bubbles are seen in the ~125 nm wide figure. The bubbles range in size from 1.2 nm to 4 nm, with an average diameter of <d> = 1.8 nm. There does not appear to be a periodic spacing between the bubbles. However, interphase boundaries are difficult to image using conventional TEM due to spherical aberrations and defocus effects. It is possible that under-focusing the beam caused some He bubbles to

appear grouped as one large bubble (such as the horizontally elongated red bubble in the center of Figure 4). Furthermore, no bubbles were observed in the YTO substrate. It is possible that no He entered the YTO through the interface or the He diffused out of the YTO all together. Alternatively, the He in the YTO may be dissolved throughout the structure, or the He bubbles are too small to see in TEM. More quantitative measurements of the He depth profile are required. Secondary ion mass spectroscopy (SIMS) was used to measure the He concentration in the YTO, but the results were inconclusive and thus not reported here.

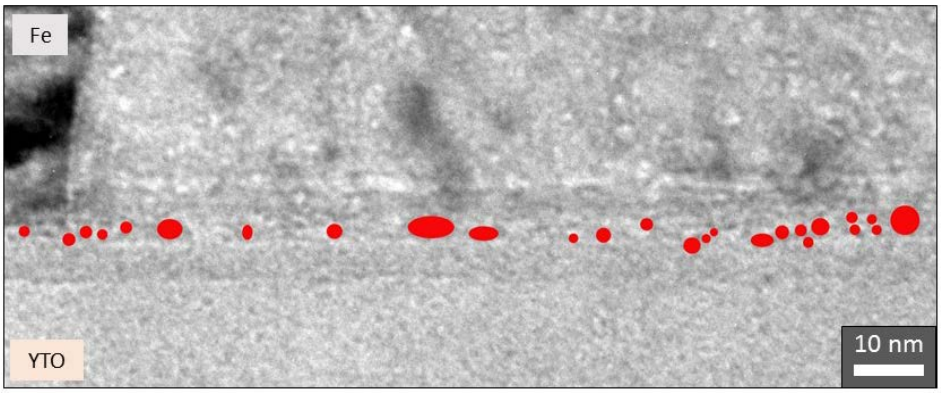

Figure 4. Under-focus TEM image from the Fe-YTO bilayer. Red circles show the sizes and locations of He bubbles at the Fe-YTO interface. No bubbles were observed in the YTO.

Three random Fe grains were chosen for bubble analysis. They have slightly different ORs. The nine graphs in Figure 5 show the average He bubble size <d>, number density <N>, and volume fraction <f> for three random areas in the Fe film. A depth of 0 nm indicates the top surface of the grain, while 200 nm indicates the bottom near the Fe-YTO interface. The bubble size graphs for the three areas are all plotted on the same scale to allow for direct comparison. The same is true for number density and volume fraction graphs.

Area 1 had the largest bubbles with an average size of <d> = 1.7 nm, while Area 2 had <d> = 1.4 nm bubbles, and Area 3 had <d> = 1.5 nm bubbles. All three areas show a roughly flat bubble size profile, with smaller bubbles at the top of the Fe and at the Fe-YTO interface. The average bubble size in all three Fe areas are smaller than at the interface where <d> = 1.8 nm.

The number density plots follow a u-shape trend. <N> is large at shallow depths into the Fe (except for Area 1), is minimum at ~ 50 nm, and steadily increases towards the Fe-YTO interface. Overall, Area 3 had the largest number density of bubbles compared to Areas 1 and 2. The third column of graphs indicates an increase in bubble volume fraction as a function of depth. For all three graphs, the average volume fraction is ~ 0.2% at the top of the grain, and the value increases with depth. In Area 1, <f> has a maximum value of 0.45% at 150 nm, then drops to 0.2% at 170 nm. Area 2 has a maximum <f> of 0.32% at 175 nm. Area 3 had the largest overall volume fraction of bubbles, with a maximum of 0.48% at 130 nm into the Fe. This depth is consistent with the expected He concentration profile calculated by SRIM. The He profiles are different between the three areas likely due to the Fe grains not having the same orientation with respect to the He implantation beam axis.

Summary and Future Studies

In summary, a YTO single crystal was cut, polished, and cleaned in preparation for deposition. 20 nm of Fe was deposited using MBE, followed by 200 nm of electron beam deposited Fe. The sample was then capped with 5 nm of AlO_x and coated with 9 nm of Pt. EBSD analysis showed sub-micron Fe grains with an axiotaxial orientation relationship with the underlying {110}YTO substrate. The bilayer was then implanted with 25 keV He with a dose of 4E15 He/cm^2. TEM images show a range of He bubble sizes, number densities, and volume fractions. The bubbles within the Fe grains ranged in size among the three areas studied, but the bubbles at the interface were overall larger with an average size of <d> = 1.8 nm. No bubbles were seen in the YTO substrate, however, this does not indicate that He was not present in the YTO. The bilayers are being prepared for future He implantation studies. The results will help inform first principle models of metallic oxide interfaces, as well as reaction-rate theory models for predicting NFA behavior.

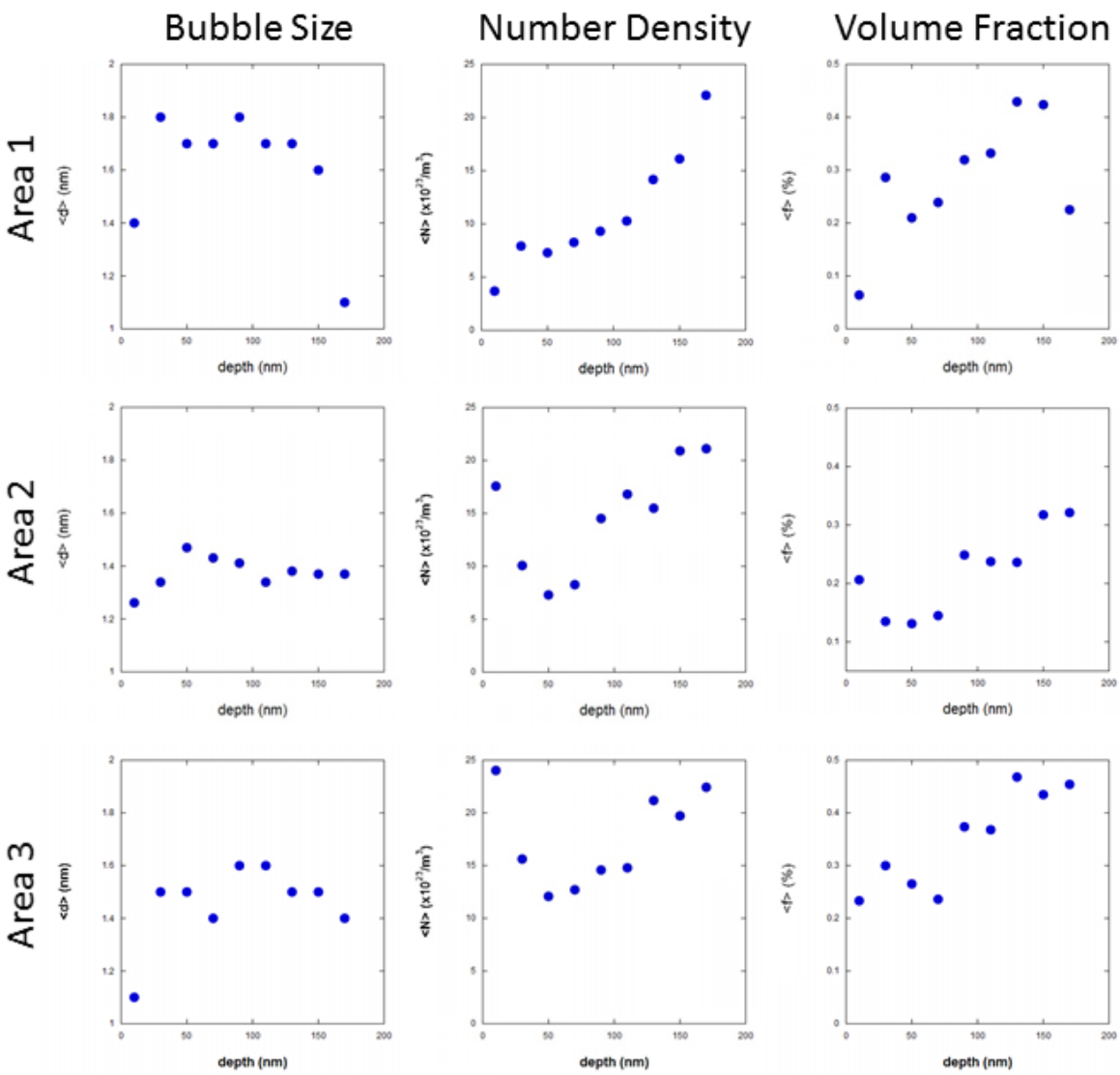

Figure 5. Graphs showing the average He bubble size <d>, number density <N>, and volume fraction <f> for three analyzed areas (Area 1, 2, and 3).

References

[1] G.R. Odette, J. of Mater., 66, 12, (2014) 2427.
[2] G.R. Odette, M.J. Alinger, B.D. Wirth, Annu. Rev. Matter. Res. 38 (2008) 471.
[3] Y. Dai, G.R. Odette, T. Yamamoto, Comp. Nuc. Mat. (2012) Elsevier.
[4] K. Dawson, G.J. Tatlock, J. Nuc. Mat. 444 (2014) 252.
[5] J. Ribis, Y. de Carlan, Acta Mat. 60 (2012) 238.
[6] J. Ciston, Y. Wu, G.R. Odette, et al., Fus. Mat. Semiann. Prog. Rep. (2012) DOE-ER-0313/51.
[7] T. Stan, Y. Wu, G.R. Odette, et al., Metal. and Mater. Trans. A, 44, 10 (2013) 4505.
[8] T. Stan, Y. Wu, G.R. Odette, Fus. Semiann. 56 (2013) DOE-ER-0313/56.
[9] T. Stan, Y. Wu, S. Kraemer, et al., Fus. Semiann. 57 (2014) DOE/ER-0313/57.
[10] T. Stan, Y. Wu, G.R. Odette, et al. Fus. Semiann. 58 (2015) DOE/ER-0313/58.